



Available online at www.sciencedirect.com

ScienceDirect

Comput. Methods Appl. Mech. Engrg. 344 (2019) 164–185

Computer methods in applied mechanics and engineering

www.elsevier.com/locate/cma

Topology optimization of conformal structures on manifolds using extended level set methods (X-LSM) and conformal geometry theory

Qian Yea, Yang Guob, Shikui Chena,*, Na Leid, Xianfeng David Gub,c

^a Department of Mechanical Engineering, State University of New York at Stony Brook, United States
 ^b Department of Computer Science, State University of New York at Stony Brook, United States
 ^c Department of Applied Mathematics and Statistics, State University of New York at Stony Brook, United States
 ^d DUT-RU International School of Information Science & Engineering, Dalian University of Technology, China

Received 4 May 2018; received in revised form 25 August 2018; accepted 31 August 2018 Available online 10 October 2018

Abstract

In this paper, we propose a new method to systematically address the issue of structural shape and topology optimization on free-form surfaces. A free-form surface, also termed manifold, is conformally mapped onto a 2D rectangle domain where the level set function is defined. With the conformal mapping, the covariant derivatives on the manifold can be represented by the Euclidean gradient operators multiplied by a scalar. Keeping this intrinsic relation in mind, we derive the Euclidean form for the Riemannian Hamilton–Jacobi equation governing the boundary evolution on the manifold, which can be solved on a 2D plane using classical level set methods, such as the upwind finite difference or fast marching method. By reducing the dimension of the problem, the topology optimization problem on the manifold embedded in the 3D space can be recast as a 2D topology optimization problem in the Euclidean space. Compared with other approaches which need project the Euclidean differential operators to the manifold, the proposed method can not only reduce the computational cost but also preserve all the advantages of conventional level set methods. The proposed method reveals the fundamental relation between topology optimization on manifolds and Euclidean planes. It provides a unified level-set-based computational framework for the generative design of conformal structures with increasing applications in different fields of interests.

© 2018 Elsevier B.V. All rights reserved.

Keywords: Topology optimization; Level set methods; Conformal mapping; Free-form surface; Manifold; Partial differential equations

1. Introduction

1.1. Topology optimization on surfaces: State of the art

Topology optimization is an optimization-driven method capable of generating an optimal design without depending on the designers' intuition, experience, and inspiration. Topology optimization is playing a crucial and

E-mail address: shikui.chen@stonybrook.edu (S. Chen).

^{*} Corresponding author.

rapidly expanding role for design innovation in the 3D printing age. As an important subcategory of topology optimization, topology optimization of shell structures has been extensively studied for their broad applications both in academia and industry, for example, architectural design [1], conformal flexible electronics [2,3], automotive and aviation structure design [4], and so on. Recently, with the maturation of additive manufacturing (AM) technologies which can provide the designers with extra design freedom when paired with topology optimization, people's desires to obtain conformal shell structure designs on free-form surfaces have been inflated. One trend of the pioneering research is to optimize the laminated composite shells. Lund and Stegmann et al. [5-7] presented a new method for concurrently optimizing the material distribution and fiber orientation on a fixed design domain. In contrary to the fiber-reinforced method which assumes shells with a fixed thickness and shape [5-7], the element-based topology optimization approaches, such as the homogenization-based topology optimization method [8–10] or the Solid Isotropic Material with Penalization (SIMP) method [11,12], can optimize the shell thickness distribution and its shape. In particular, the SIMP-based topology optimization method has gained significant popularity. Fauche et al. [13] employed SIMP method to optimize the material distribution for a thin-shell bridge. Nakayama and Shimoda [14] proposed a method for simultaneous shape and topology optimization of shell structures, which improved the numerical stabilities by coupling the H^1 gradient-based approach with the SIMP method. Later, Ansola et al. [15] devised an integrated framework to find the optimum shape and material layout on a shell structure. In a later contribution, Ansola extended this work to simultaneously optimize the shape and reinforcement layout on a surface [16]. In order to optimize on general surfaces, Hassani et al. [17] introduced the Non-Uniform Rational B-Spline (NURBS) technology into the SIMP model for the surface generation. In spite of the aforementioned advantages, the SIMP-based topology optimization is vulnerable to checkerboard patterns caused by numerical instabilities [18]. Therefore, post-processing approaches, such as the noise cleaning technique [17], automated image interpolation methods [19,20], neural networks [21], or support vector machine (SVM) [22], oftentimes have to be employed to convert the density results into crisp designs. Alternatively, minimum length scale constraints, as proposed by Guest [23], or the Monotonicity based minimum LEngth scale (MOLE) method [24], can also be employed to regulate the designs for better final optimization results.

Compared with the aforementioned element-based methods, the level set methods and some recently developed explicit approaches, such as Moving Morphable Components (MMC) [25–27], Moving Morphable Void (MMV) [28] or the geometry projection method [29–31], can provide a design with clear boundaries. Those explicit methods have demonstrated superiority in handling design-dependent problems, as well as better compatibility with manufacturing. Moreover, higher-order geometric information, such as normal vectors or curvatures, is naturally embedded in the geometric level set model [32–35]. Such information can be utilized to realize direct integration between topology optimization and additive manufacturing [36], which makes the level-set-based topology optimization approach a powerful tool for generative design.

However, conventional level set functions are defined in Euclidean space \mathbb{R}^2 or \mathbb{R}^3 on a fixed Cartesian coordinate system. To meet the demand of doing topology optimization on free-form surfaces, the conventional level-set-based topology optimization methods need to be extended from Euclidean space to Riemann surfaces.

1.2. Solving partial differential equations (PDEs) on manifolds

As a PDE-driven approach [37], level-set-based topology optimization on manifolds is essentially a variational problem on surfaces, which has been studied in the field of differential geometry and applied to computer graphics. One popular method for solving such problems is based on numerical approximation, where the manifold is discretized to a triangle mesh [38], point sets [39], NURBS or B-spline [40,41], and the solution to the global PDEs is approximated by solving local PDEs on each segment. Recently, the NURBS-based Isogeometric Analysis (IGA) method has been employed for solving higher-order PDEs on manifolds [40,41]. The numerical approximation approach is straightforward and can be conveniently integrated with commercial FEA or CAD solvers.

An alternative way to solve PDEs on surfaces is the so-called embedding method. Its key idea is to construct a space surrounding the manifold in \mathbb{R}^3 , either explicitly (the closest point method [42]) or implicitly (level set methods [43]), and then replace the PDEs on the surface with its standard representation defined in \mathbb{R}^3 . Ruuth et al. [42] employed the closest point method to numerically approximate PDEs on a surface as close as possible with PDEs defined in \mathbb{R}^3 . This embedding approach is efficient due to the reason that the computation is only carried out on a grid near the surface [42,44]. However, since the embedding PDE is only valid initially, an extension step is needed to ensure

the computational accuracy. Macdonald and Ruuth [45] combined the closest point method with level set methods to evolve the interfaces on general surfaces. Similar to the closest point method, the implicit method uses an embedding PDE defined in the embedding space. While the embedding space is defined implicitly in one higher dimension by using level set representations, and the PDEs are solved in the Cartesian coordinate system [46,43,47]. This approach is both robust and accurate in dealing with deforming surfaces. Chen et al. [48] utilized the variational method [43,49] to identify the point-wise correspondence of the material during the level set evolution. Nonetheless, as stressed in the work of King et al. [44], the implicit method cannot handle complex surfaces as the closest point method does.

In this paper, we employ conformal mapping [50,51] to solve PDEs on manifolds, which can be explicitly calculated using the conformal geometry theory [52,53]. With conformal parameterization, a manifold is mapped to a 2D domain. Meanwhile, the corresponding covariant derivatives on a surface can be represented by the Euclidean differential operators multiplied by a scalar factor [54]. By reducing the dimension of the problem, the variational problems defined on a 3D surface is transformed into a variational problem on a 2D plane. The proposed method not only reduces the computing cost but also lowers the implementation complexity of the algorithm. More importantly, it reveals the intrinsic relation between topology optimization on Euclidean planes and manifolds, which offers us a significant advantage to reformulating the level-set-based topology optimization problem on a free-form surface as a 2D problem in the Euclidean space. Consequently, we propose a new computational framework to systematically address the problem of structural shape and topology optimization on manifold using level set methods and conformal mapping theory. The major contribution is that we extend the conventional level-set-based topology optimization method from Euclidean space to free-form surfaces with arbitrary topologies.

The paper is organized as follows: Section 2 introduces the background regarding conventional level set methods. Section 3 presents the conformal mapping theory. In Section 4, we formulate the mean compliance optimization problem on the surface and derive the shape sensitivity equations. The algorithm and the implementation of our extended level set method (X-LSM) are presented in Section 5, followed by the four demonstration examples in Section 6. In Section 7, a mechanics experiment has been carried out to validate the performance of a thin-shell structure with optimized conformal ribs. Section 8 summarizes the paper, discussing the pros and cons of the proposed method and outlining the future work.

2. Method overview

The proposed method combines the level-set-based topology optimization approach with the conformal mapping theory. Using conformal mapping, the geometric information is transported between the manifold and the 2D computational domain in the Euclidean space. The level set function is defined on the 2D domain and evolved by solving the modified Hamilton–Jacobi equation. The sensitivity analysis is calculated using the adjoint sensitivity analysis method. The structure performance is evaluated using finite element analysis (FEA), where the 3D manifold is modeled as a linear elastic thin shell structure. It is worth noting that the FEA can also be done in the 2D plane using the conformal mapping, which is beyond the current scope of this paper. The flowchart is shown in Fig. 1. By extending the conventional level-set-based topology optimization framework to manifolds, the proposed method can directly achieve optimal design on surfaces with arbitrary topologies. The key advantages of the method are threefold:

- 1. **General**: the method is valid to free-form surfaces with arbitrary topologies. In addition, the method is not only designed for the minimum compliance problem but also can be easily transformed to solve other topology optimization problems with different objective functions and constraints.
- 2. **Compatible**: the proposed method can be easily coupled with the conventional level set framework and is well compatible with finite element analysis methods. With the proposed method, researchers can take full advantage of existing level-set-based topology optimization codes without needing to start from scratch.
- 3. **Efficient**: with conformal parameterization, the 3D shell structure optimization problem is solved on the 2D domain, which greatly reduces the computing costs. Besides, with the conformal mapping theory, the derived formulation of the covariant derivatives in Euclidean space is in the simplest form and thus easy to calculate.

2.1. Classical level set methods

Conventionally, the level set function ϕ is a Lipschitz continuous real-valued function defined in \mathbb{R}^n [32]. The boundary of the design $\partial \Omega$ is implicitly represented as the zero level set of the function ϕ , as demonstrated in Fig. 2.

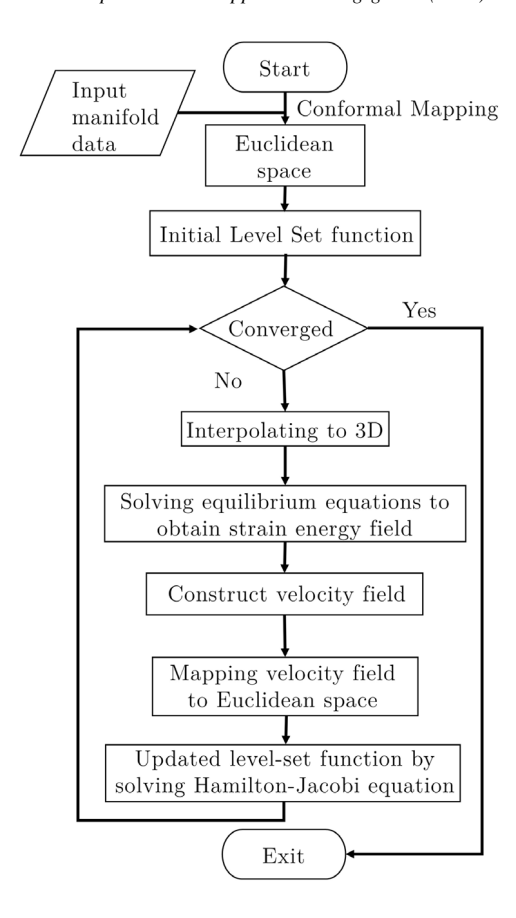


Fig. 1. The flow chat of X-LSM.

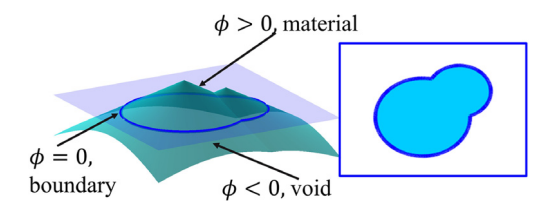


Fig. 2. A schematic of level set representation.

By cutting the level set function at the zero level, the whole computational domain D is defined as three parts according to the value of the level set function, which are the material, the boundary, and the void, respectively. The properties of the level set function can be formulated as Eq. (1):

$$\begin{cases} \phi(\mathbf{x}, t) > 0, & x \in \Omega, \text{ material} \\ \phi(\mathbf{x}, t) = 0, & x \in \partial \Omega = \Gamma(t), \text{ boundary} \\ \phi(\mathbf{x}, t) < 0, & x \in D/\Omega, \text{ void} \end{cases}$$
 (1)

where \mathbf{x} is the spatial coordinate of a point inside the computational domain; t represents the time; $\Gamma(t)$ is the dynamic boundary of the design. Embedding the design in one higher dimension allows the flexibility in topological changes such as boundary merging or splitting in the design process while keeping the boundary of the design clearly defined.

The boundary evolution is governed by the Hamilton–Jacobi (H–J) equation as Eq. (2) shows [55]:

$$\frac{\partial \phi}{\partial t} - \mathbf{V} \cdot \nabla \phi = 0, \tag{2}$$

where $\mathbf{V} = \dot{\mathbf{x}}$ is the velocity field.

3. Conformal mapping theory

The conventional level-set-based topology optimization method is a PDE-driven approach [37]. In order to extend the level set approach to manifolds, we first formulate the new H–J equation which governs the boundary motion on the manifold. Then, we transform the PDE from the manifold into the 2D Euclidean plane where the modified H–J equation can be solved with conventional upwind finite difference schemes [56] or fast marching method [57]. The complexity of the modified H–J equation depends on the parameterization of the manifold, which may result in derivative terms and non-constant coefficients [52]. By applying conformal parameterization that preserves angles, the formula of the covariant derivative is simple and similar to the usual Euclidean ones [58,54]. Thus, it brings great advantage in solving the modified H–J equation with conventional level set schemes in \mathbb{R}^2 or \mathbb{R}^3 , and at the same time, greatly reduces the computational complexity.

This section presents the theoretical background of conformal mapping. Moreover, the differential operators and the H–J equation on manifolds with conformal parameterization are introduced. The algorithm for computing the conformal mappings rests on Hamilton's Ricci flow theory [59], which has been applied for the proof of Poincaré's conjecture. The discrete Ricci flow theory is based on the variational principle on polyhedral surfaces. The basic theory of discrete Ricci flow is introduced in Appendix B. For more details on Ricci flow, we refer the interested readers to the paper [60]. A complete survey on numerical algorithms of conformal mapping can be found in the paper [61].

3.1. Conformal mapping of Riemann surfaces

The conformal mapping theory originates from differential geometry on the Riemannian manifold [58]. Specifically, a Riemannian manifold is defined as a smooth manifold M with a given Riemannian metric \mathbf{g} , which is normally a 2D symmetric tensor field [62]. We can consider the Riemannian metrics as objects which describe the length of the tangent vectors and the length of the curves on the Riemannian manifold. Suppose given two Riemannian surfaces $(S_1, \mathbf{g_1})$ and $(S_2, \mathbf{g_2})$, where $\mathbf{g_1}$ and $\mathbf{g_2}$ are Riemannian metric tensors, a C^1 smooth mapping $\varphi: S_1 \to S_2$ is called *conformal* if the pull-back metric induced by φ and the original metric on the source differ by a scalar function. Specifically, there exists a real function $\lambda: S \to \mathbb{R}$, such that

$$\varphi^* \mathbf{g_2} = e^{2\lambda} \mathbf{g_1},$$

where λ is the conformal factor quantifying the scaling effect of the conformal mapping.

Thus, intuitively, the derivative map $d\varphi: TS_1(p) \to TS_2(\varphi(p))$ is a scaling transformation, which maps infinitesimal circles to infinitesimal circles. As shown in Fig. 3, a surface is conformally mapped onto a 2D disk, and the infinitesimal circles on the surface as Fig. 3a are preserved on 2D as Fig. 3b. Therefore, φ preserves angles.

In conclusion, the conformal mapping can be considered as a local scaling process governed by the scalar function $e^{2\lambda}$. The Riemannian metric of conformal mapping has a simple formula related to the conformal factor. It is proven in [52] that by using conformal mapping the covariant derivatives on the surface in \mathbb{R}^3 are equivalent to the Euclidean gradient operators apart from the scalar function. Thus, with conformal mapping, PDEs on surfaces can be formulated to 2D with modified variational operators. For example, at each point $p \in (S, \mathbf{g})$, there is a neighbor U(p), which can be conformally mapped onto the unit disk \mathbb{D}^2 on the plane. Suppose the planar coordinates are (u, v), then the Riemannian metric can be written as

$$\mathbf{g} = e^{2\lambda(u,v)}(du^2 + dv^2),$$

where (u, v) is called the *isothermal parameters* of the surface.

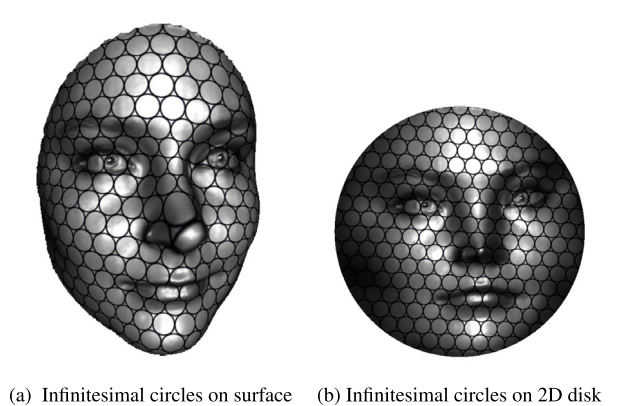


Fig. 3. Conformal mapping from the 3D surface to the 2D disk preserves infinitesimal circles.

3.2. Differential operators on Riemannian surfaces

Given a Riemannian surface S and $\varphi: \mathbb{R}^2 \to S$ is a conformal mapping and an arbitrary function $f: S \to \mathbb{R}$ which is defined on the manifold, we can reparameterize f with φ , so that its derivatives can be easily calculated on the 2D Euclidean space \mathbb{R}^2 . Suppose the conformal factor of φ is $e^{2\lambda}$, we can define the partial derivative of f respect to $x \in S$ as [54,52]:

$$\partial_{x} f = \lim_{\Delta x \to 0} \frac{f \circ \varphi(x + \Delta x, y) - f \circ \varphi(x, y)}{d_{S}(x + \Delta x, x)}$$

$$= \lim_{\Delta x \to 0} \frac{f \circ \varphi(x + \Delta x, y) - f \circ \varphi(x, y)}{\sqrt{e^{2\lambda}} \Delta x}$$

$$= e^{-\lambda} \frac{\partial f \circ \varphi}{\partial x},$$
(3)

where $d_S(x, y)$ is the distance between $x, y \in S$ and $f \circ \varphi = f(\varphi(x, y))$. Similarly, we can define the partial derivative of f with respect to y

$$\partial_{y} f = \lim_{\Delta y \to 0} \frac{f \circ \varphi(x, y + \Delta y) - f \circ \varphi(x, y)}{d_{S}(y + \Delta y, y)}$$

$$= \lim_{\Delta y \to 0} \frac{f \circ \varphi(x, y + \Delta y) - f \circ \varphi(x, y)}{\sqrt{e^{2\lambda}} \Delta y}$$

$$= e^{-\lambda} \frac{\partial f \circ \varphi}{\partial y}.$$
(4)

The gradient of f can be derived based on

$$\nabla_g f = \partial_x f \mathbf{i} + \partial_y f \mathbf{j},\tag{5}$$

where

$$\mathbf{i} = \frac{\partial}{\sqrt{\langle \frac{\partial}{\partial x}, \frac{\partial}{\partial x} \rangle} \partial x} = e^{-\lambda} \frac{\partial}{\partial x},$$

$$\mathbf{j} = \frac{\partial}{\sqrt{\langle \frac{\partial}{\partial y}, \frac{\partial}{\partial y} \rangle} \partial y} = e^{-\lambda} \frac{\partial}{\partial y}.$$

Therefore, the Riemannian gradient defined on manifolds can be expressed in terms of Euclidean differential operators, as shown in Eq. (6):

$$\nabla_g f = e^{-2\lambda} \frac{\partial f \circ \varphi}{\partial x} + e^{-2\lambda} \frac{\partial f \circ \varphi}{\partial y},\tag{6}$$

which lays the mathematical foundation for the modified H-J equation.

3.3. Modified Hamilton-Jacobi equation

Following the conformal geometry theory, we can conformally parameterize the manifold onto a 2D rectangular domain and evolve the level set function on the plane to optimize the design. Given a level set function $\phi(\mathbf{x}, t)$, the boundary is defined as the zero level set, that is,

$$\phi(\mathbf{x},t) = 0. \tag{7}$$

Conventionally, the H–J equation is achieved by differentiating Eq. (7) with respect to time t. Similarly, as explained in Section 3, we can derive the H–J equation on surface with the Riemannian gradient, as formulated in Eq. (8):

$$\frac{\partial \phi}{\partial t} - \dot{\mathbf{x}} \cdot \nabla_g \phi = 0, \tag{8}$$

where $\dot{\mathbf{x}}$ is the continuous velocity field in the local tangential plane to the manifold; $\nabla_g \phi$ is the Riemannian gradient of ϕ on the manifold. The scalar form of Eq. (8) can be rewritten as follows:

$$\frac{\partial \phi}{\partial t} - v_n |\nabla_g \phi|_g = 0, \tag{9}$$

where v_n is the normal velocity field on the manifold.

Let f be the conformal mapping between a manifold M and a 2-D domain: $f: M \to \mathbb{R}^2$. Following the conformal geometry theory [58,54], we can use Eq. (6) to formulate the relation between the Riemannian gradient $\nabla_g \phi$ and its Euclidean counterpart $\nabla \phi$ as Eq. (10):

$$|\nabla_g \phi|_g = e^{-\lambda} |\nabla \phi|,\tag{10}$$

where the λ is the conformal factor. By substituting Eq. (10) into Eq. (8), we can deduce the Euclidean representation of the level set equation on the manifold:

$$\frac{\partial \phi}{\partial t} - e^{-\lambda} v_n |\nabla \phi| = 0. \tag{11}$$

We define Eq. (11) as the *modified Hamilton–Jacobi equation*. In this way, the problem of boundary evolution on the manifold can be equivalently solved on the 2D domain with the modified H–J equation. It is also worth noting that only with the conformal mapping we can attain such a concise Euclidean representation of the level set equation on the manifold, which otherwise would be extremely complex and computationally formidable.

4. Level-set-based topology optimization on surfaces

4.1. Problem formulation

In this study, the structural stiffness of a free-form surface is optimized subject to a volume constraint. The free-form surface is modeled as a linear elastic thin-shell structure using finite element method. The optimization problem is formulated as follows:

Minimize :
$$J = \int_{\Omega} \epsilon_{ij}(u) \mathbb{C}_{ijkl} \epsilon_{kl}(u) d\Omega$$
,
Subject to : $a(u, v) = l(v)$, $\forall v \in U_{ad}$

$$V(\Omega) = V^*.$$
(12)

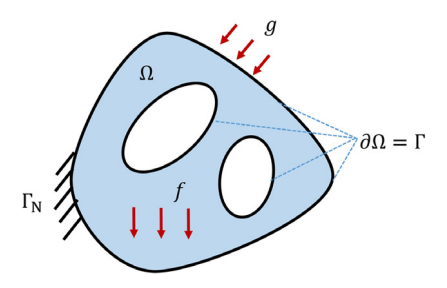


Fig. 4. A schematic of general boundary conditions.

where U_{ad} is the space kinematically admissible displacement [63], V denotes the volume of the manifold shell; V^* stands for the target volume; ϵ is the linear strain tensor. \mathbb{C}_{ijkl} is the fourth-order constitutive tensor; Ω is the region occupied with the linear elastic material. The volume $V(\Omega)$, internal virtual energy a(u, v), and exterior virtual energy l(v) are defined as follows:

$$V(\Omega) = \int_{D} H(\phi) d\Omega,$$

$$a(u, v) = \int_{\Omega} \epsilon_{ij}(u) \mathbb{C}_{ijkl} \epsilon_{kl}(v) d\Omega,$$

$$l(v) = \int_{\Omega} f \cdot v d\Omega + \int_{\Gamma_{N}} g \cdot v d\Gamma,$$

where D is the design domain; $\Gamma = \partial \Omega$ is the boundary of the design; a(u, v) is a symmetric bilinear function in terms of the displacement u and the test function v, that is, a(u, v) = a(v, u); l is a linear function in terms of the body force f and the traction force g on the Neumann boundary conditions Γ_N , as illustrated in Fig. 4.

4.2. Shape sensitivity analysis

In this section, the shape sensitivity analysis is derived using the adjoint sensitivity analysis. The first step is to formulate the Lagrangian of the optimization problem [25,35,64,65]:

$$L(u, v) = J + a(u, v) - l(v) + \lambda(V(\Omega) - V^*), \tag{13}$$

where the λ is a Lagrange multiplier, and v becomes the adjoint displacement in the adjoint sensitivity analysis. Eq. (13) can be reformulated as:

$$L(u, v) = a(u, u) + a(u, v) - l(v) + \lambda(V(\Omega) - V^*).$$
(14)

The material derivative of Eq. (14) with respect to a pseudo time t is formulated as follows [63,66,67]

$$\frac{dL(u,v)}{dt} = \frac{\partial L(u,v)}{\partial t} + \frac{\partial L(u,v)}{\partial \Omega},\tag{15}$$

where the partial derivative with respect to time results in the so-called adjoint equation:

$$\frac{\partial L(u,v)}{\partial t} = L' = a'(u,u) + a'(u,v),\tag{16}$$

and

$$a'(u, u) = 2 \int_{\Omega} \epsilon_{ij}(u') \mathbb{C}_{ijkl} \epsilon_{kl}(u) d\Omega,$$

$$a'(u, v) = \int_{\Omega} \epsilon_{ij}(u') \mathbb{C}_{ijkl} \epsilon_{kl}(v) d\Omega.$$
(17)

The convection term of the material derivative forms the shape derivative which is formulated as follows:

$$\frac{\partial L(u,v)}{\partial \Omega} = \int_{\Gamma} \epsilon_{ij}(u) \mathbb{C}_{ijkl} \epsilon_{kl}(u) v_n ds + \int_{\Gamma} \epsilon_{ij}(u) \mathbb{C}_{ijkl} \epsilon_{kl}(v) v_n ds
- \int_{\Gamma} f \cdot v v_n ds - \int_{\Gamma} \left[\frac{\partial (g \cdot v)}{\partial n} + \kappa g \cdot v \right] v_n ds + \lambda \int_{\Gamma} v_n ds.$$
(18)

Solving Eq. (16), we can get the adjoint variable v = -2u. Substitute v = -2u to Eq. (18) and ignore the body force, we can get

$$\frac{\partial L(u,v)}{\partial \Omega} = \int_{\Gamma} [\epsilon_{ij}(u) \mathbb{C}_{ijkl} \epsilon_{kl}(u) + \lambda] v_n ds. \tag{19}$$

By using the steepest-descent method, we can construct the normal velocity field as

$$v_n = -\epsilon_{ij}(u)\mathbb{C}_{ijkl}\epsilon_{kl}(u) - \lambda, \tag{20}$$

where the first term $\varepsilon_{ij}(u)\mathbb{C}_{ijkl}\varepsilon_{kl}(u)$ is the strain energy density of the linear elastic structure. Specifically, the explicit expression of Eq. (20) can be derived from the shell formulation [63] as follows

$$v_n = -\left[2\epsilon_{ij}^1(u)\mathbb{C}_{ijkl}\epsilon_{kl}^1(u)|\mathbf{J}| + \frac{2}{3}\epsilon_{ij}^2(u)\mathbb{C}_{ijkl}\epsilon_{kl}^2(u)|\mathbf{J}|\right] - \lambda,\tag{21}$$

where $\epsilon_{ij}^1(u)$ and $\epsilon_{ij}^2(u)$ are the membrane-shear stain and bending strain respectively. The first term of Eq. (21) denotes the displacement of the middle shell surface. The bending and shear deformation represents the rotation of the cross section. In this paper, for simplicity, the volume constraint is handled by using the fixed Lagrangian method [32]. The detailed derivation is provided in Appendix A.

5. Numerical implementation

5.1. Algorithm

In our proposed method, the geometric information is transported using conformal mapping from the manifold to the Euclidean plane, as in Section 3. Instead of solving the variation problem directly on the surface, a modified Hamilton–Jacobi equation is solved on 2D to evolve the boundary. Compared with other methods, the proposed method can guarantee a lower computational cost when optimizing the conformal surface structures.

The framework can be decomposed into seven steps as shown in Algorithm 1. The input is a triangle mesh surface S_1 . In the first step, a 2D triangular mesh rectangle Q_1 is achieved utilizing the conformal mapping parameterization. Then, we construct a 2D quad mesh on Q_1 where we define the level set function subsequently. The third step is to transport the level set values from 2D onto the surface. The level set values on the 2D triangular mesh can be interpolated from the values on the 2D quad mesh. From conformal mapping, the relationship of the vertices on S_1 and Q_1 is given, which means a vertex on Q_1 is corresponding to one specific vertex on the surface S_1 . Since the level set value on each vertex can be considered as a constant, the transportation from 2D to a surface can be naturally made by the calculated conformal mapping parameterization. Steps 4 and 5 are about to solve the equilibrium physics equations and do shape sensitivity analysis to construct the design velocity field on the surface. Next, by solving the modified H–J equation, the level set function is updated. The steps 2 through 6 are repeated until the convergence criterion is fulfilled.

Algorithm 1: A Framework for Level-Set-Based Shape and Topology Optimization on Manifold

Input: A triangle meshed surface

Output: The 3D minimum compliance design

- 1 Given S_1 , compute the global conformal parameterization from S_1 onto the 2D rectangle Q_1 ;
- 2 Initialize the level set function ϕ on the 2D rectangle domain Q_1 ;
- 3 Transport the value of ϕ onto S_1 by using Barycentric interpolation method;
- 4 Solve equilibrium equation on S_1 to obtain strain energy field;
- 5 Calculate shape sensitivity to construct the design velocity field;
- 6 Update level-set function by solving the M-H-J Equation on Q until getting converged;
- 7 Obtain the topology optimization design S_2 from ϕ ;

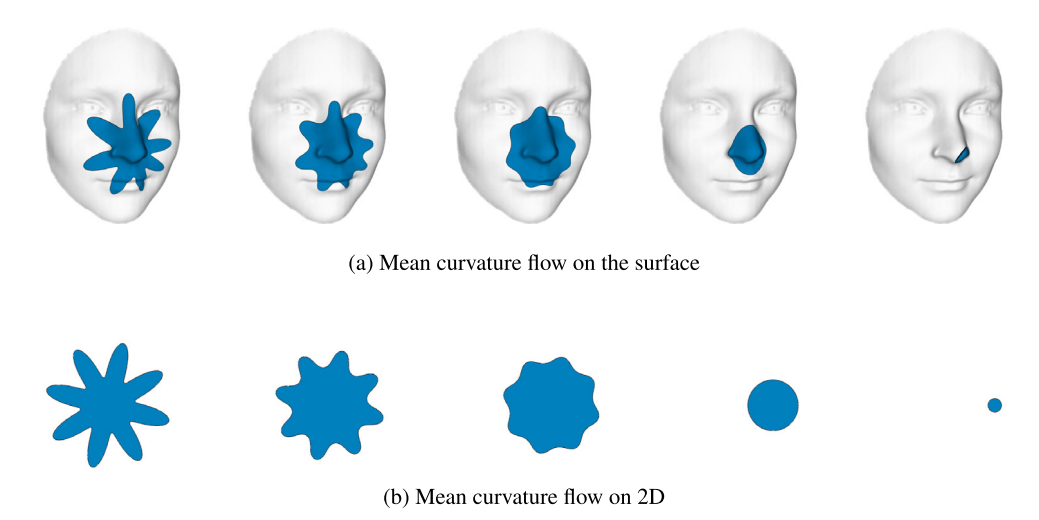


Fig. 5. Mean curvature flow on a human face surface.

6. Numerical examples

6.1. Curvature flow on surface

The mean curvature flow, also known as the curvature-shortening flow, is the most natural evolution depending on extrinsic geometry, and has been extensively studied. In this example, we test the X-LSM with the surface motion at a curvature-dependent speed:

$$v_n = -\kappa = -\nabla \cdot \mathbf{n},\tag{22}$$

where ∇ is the nabla operator and \mathbf{n} is the normal vector of the boundary. The initial boundary is a star-shape [56] on the 2D rectangular domain, as shown in Fig. 5b. By using conformal mapping, the star-shape interface is mapped to the surface, as in Fig. 5a. Eventually, on both the 2D plane and the surface, the interface morphs from a 'sunflower' to a circle and shrinks through round circles to a point until it disappears.

6.2. Convection on a torus with a constant speed

In this example, a numerical experiment of interface moving on a torus is applied to demonstrate the performance of the proposed method in handling boundary changes on manifolds with more complex topologies. As shown in Fig. 6a, a circle is moving at a constant speed on torus surface. The corresponding motion on the 2D Euclidean plane is shown in Fig. 6b, where the 2D velocity field is constant along a specified direction. By applying periodic boundary conditions, the circle can move continuously on the torus.

6.3. Topology optimization of a vase shell

In this example, we apply the X-LSM to optimize the mean compliance of a vase shape thin shell structure. The target volume ratio is 40%. The linear elastic material is assumed with a Poisson's ratio of $\nu = 0.3$ and Young's modulus E = 1 GPa. To avoid singularity, a dummy material with Young's modulus $E = 10^{-6}$ GPa is set for the void. The boundary conditions of the vase model are shown in Fig. 7. The height and width of the vase are both 0.4 m and the thickness is 0.01 m. A vertically distributed load and a moment along the z-direction are applied on the top of the vase, in which the bottom boundary is fixed.

Following Algorithm 1, we mesh the vase surface with 39 764 triangular elements and map it onto a 2D rectangle domain Q_1 . Then the level set function is constructed on Q_1 with a 75 × 101 quad mesh. The initial design domain

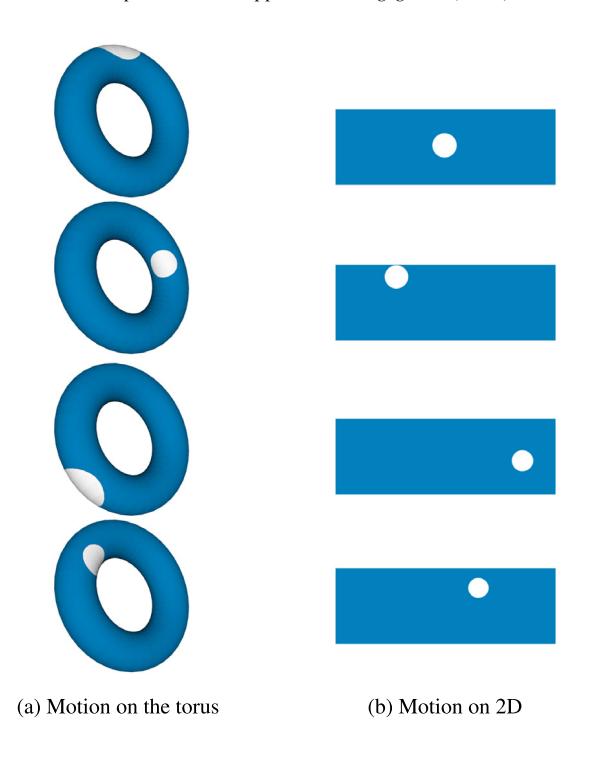


Fig. 6. Convection on a torus with a constant speed.



Fig. 7. Boundary conditions of the vase.

is set to be a surface with 40 circular holes. The topology optimization process on the 2D plane is shown in Fig. 8a, and the corresponding designs on the manifold are shown in Fig. 8b.

The optimization curve is presented in Fig. 9, where the mean compliance of the vase is minimized and the volume constraint is satisfied after 300 iterations. In addition, it is noticeable that on the vase surface the local shape of the design is preserved from the 2D design, which is consistent with the conformal mapping theory. Two prototypes have been printed using a Stratasys Connex[®] Objet260 multi-material 3D printer. The optimized vase frame, as shown in Fig. 10a, is printed using an acrylic-like material called VeroWhite. The printed result for the whole vase with the

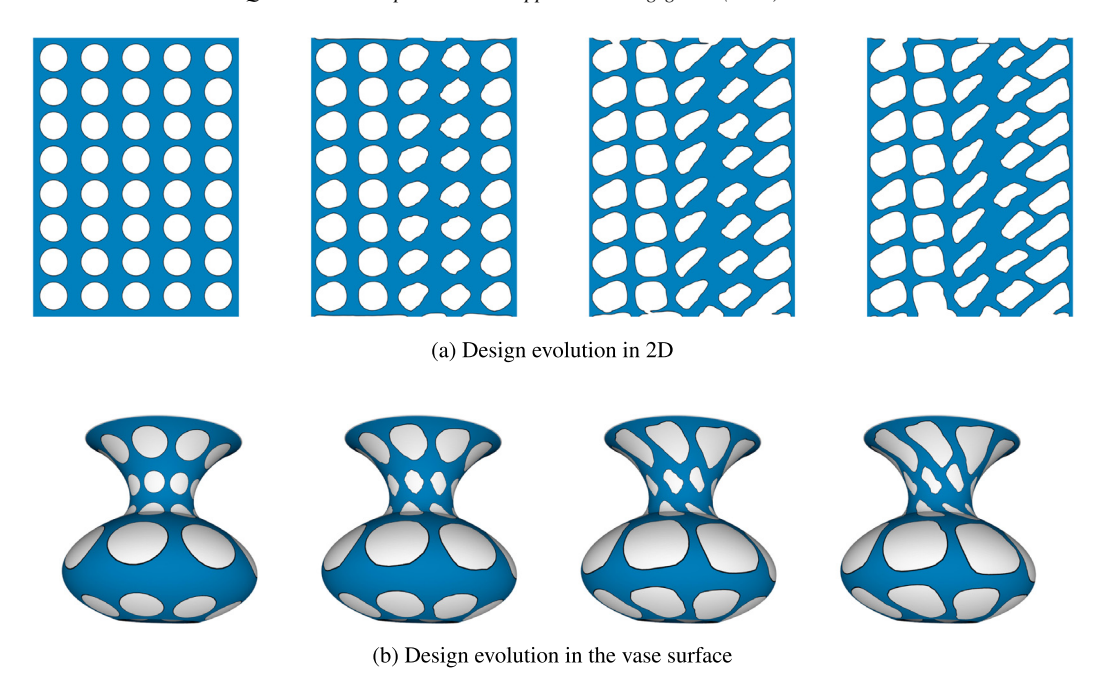


Fig. 8. Topology optimization on a vase surface.

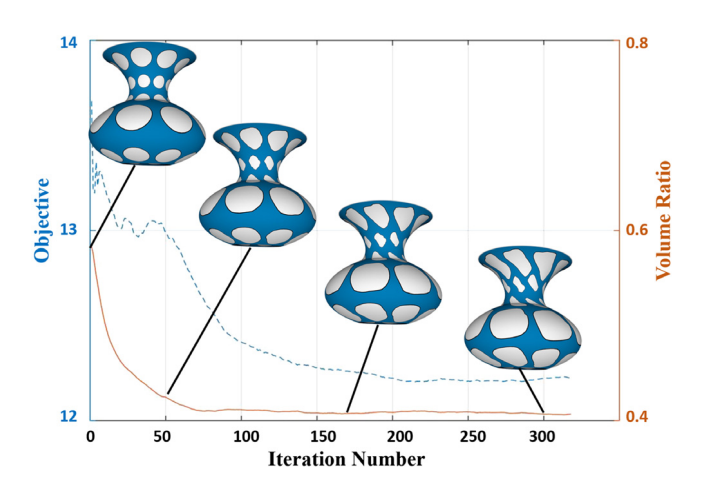


Fig. 9. The optimization history of a conformal vase frame design.

surface and frame is shown in Fig. 10b, where the frame is printed using VeroWhite, and the vase surface is printed with a transparent rubber-like material called TangoPlus.

6.4. Topology optimization of conformal reinforcement on a chair surface

In this section, we apply the X-LSM to design the conformal reinforcement structure of a chair surface. The span of the oval armchair is approximately $0.6 \text{ m} \times 0.5 \text{ m}$ and the thickness is 0.04 m. The design domain is discretized into 59 685 triangular elements. The original design and boundary conditions of the armchair surface are shown in Fig. 11. Three concentrated loads along the *z*-direction are applied at the arms and the seat area with a force on the back along the *y*-axis. In the meantime, a portion of the bottom is fixed. The target volume ratio is 40%. We minimize the mean compliance of the shell. The linear elastic material is assumed with a Poisson's ratio $\nu = 0.3$ and Young's



(a) The topology-optimized conformal frame structure of the vase



(b) The vase reinforced with the conformal frame structure

Fig. 10. The 3D-printed vase design.

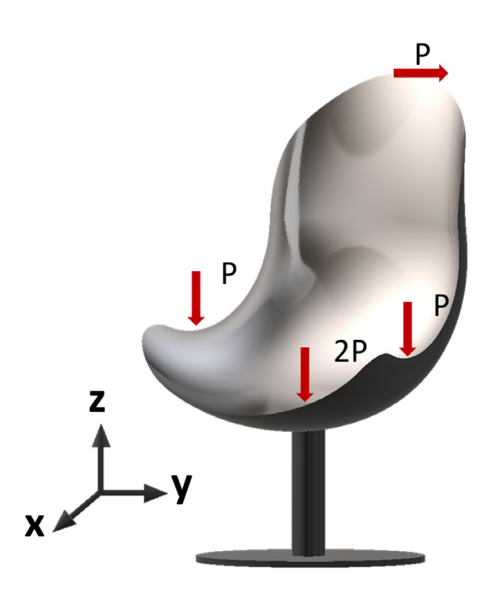


Fig. 11. Boundary conditions of the chair.

modulus E=1 GPa, and Young's modulus $E=10^{-6}$ GPa is set for the void. The initial design starts with 48 circular holes on the 2D rectangular plane which is discretized with a 120×167 quad mesh. The design evolutions in the 2D rectangular domain and on the chair surface are shown in Fig. 12. Fig. 13 shows the rendering results of the chair surface with our optimized conformal reinforcement design.

6.5. Topology optimization of a toroidal shell structure

The minimum compliance optimization problem on a toroidal shell is studied by using the same material properties as Section 6.3. The inner and outer radius of the torus is 0.1 m and 0.06 m, respectively. The shell thickness is 0.002 m. The target volume ratio is 50%. The design domain along with the boundary conditions is shown in Fig. 14a. Similarly to the vase model, a concentrated load and a moment of force along the z-direction are applied to the top of the model. A small area on the torus bottom is fixed. The surface is meshed with 3200 triangular elements, and the 2D plane is discretized with a 101×36 quad mesh. The design results are shown in Fig. 14.

7. Experiment

To validate the performance of the optimized design, we conduct a compression test on three semi-cylinder shells with different inner reinforcing structures, as shown in Fig. 15. The first one is a semi-cylinder shell structure

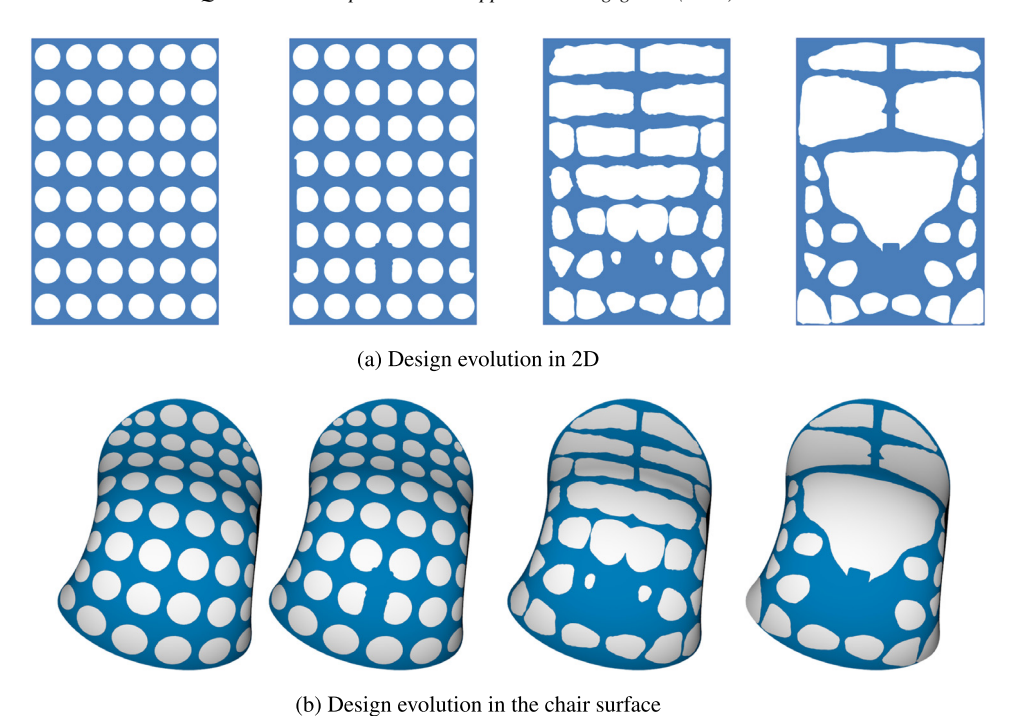


Fig. 12. Topology optimization on a conformal chair structure.

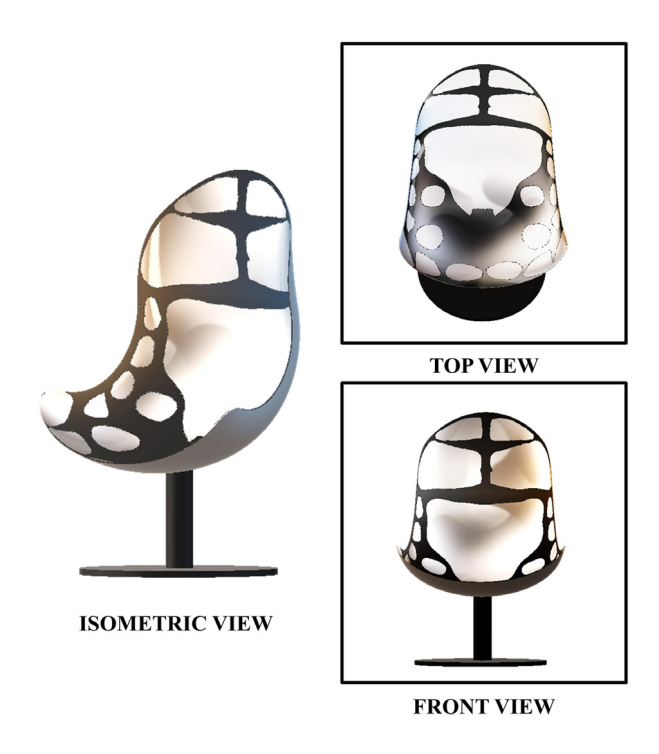
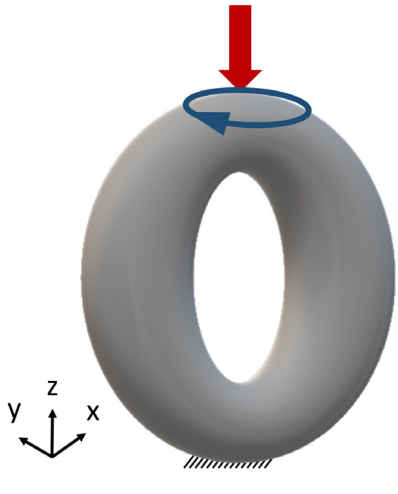


Fig. 13. Final results of the chair model.

reinforced with the optimized inner ribs obtained by the X-LSM. Other two designs are the reinforced semi-cylinder shell with conformal lattice structure structures and a uniform thickness semi-cylinder, which have been reported in



(a) Boundary conditions of the torus

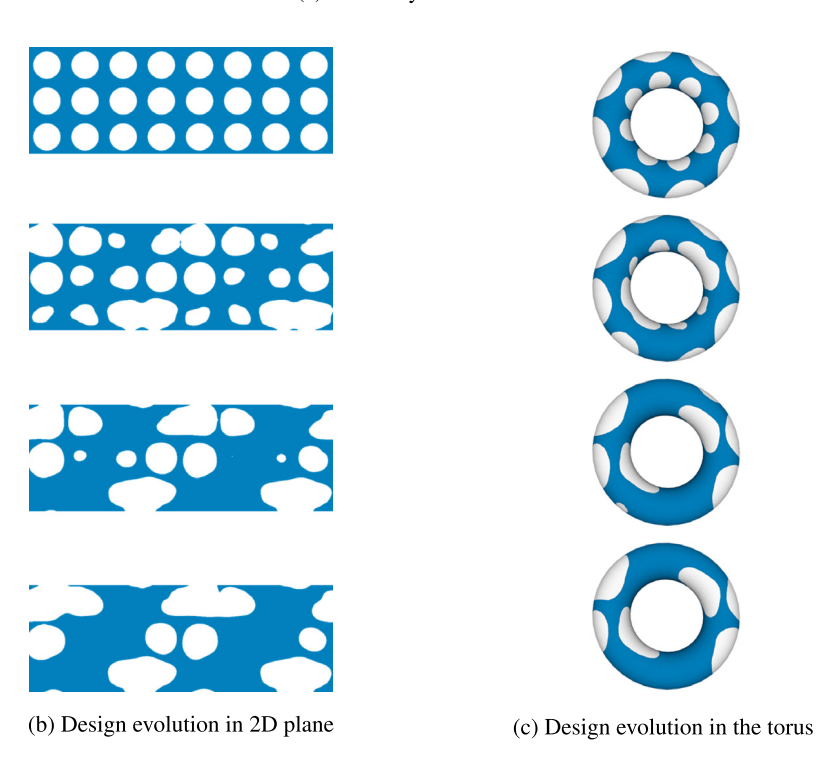


Fig. 14. Topology optimization of a toroidal shell structure.

our recent paper [68]. In order to make an apple-to-apple comparison, we follow the same experiment settings as [68], where the three semi-cylinders have same dimensions and mass.

Before doing the mechanics experiment, we first apply the X-LSM to optimize the semi-cylinder surface with a 40% volume-ratio target. The semi-cylindrical structure is fixed at the bottom with a compression on top. The optimized design is a shell structure with curved ribs connecting the top and bottom boundaries, as shown in Fig. 15(B). We can observe that the ribs have a non-uniform width, which is wider at the center area due to a higher strain energy density.

The three semi-cylinder designs with different inner structures are 3D printed using the VeroWhite material. As shown in Fig. 15, from left to right are the printed semi-cylinder shells with a conformal inner lattice structure, the

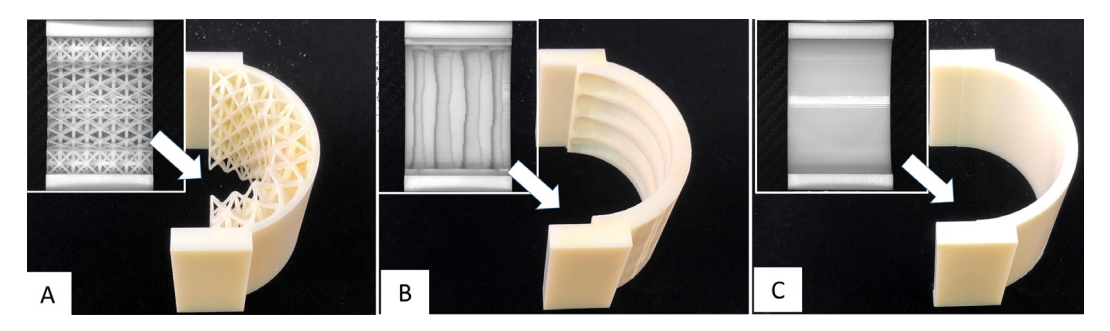


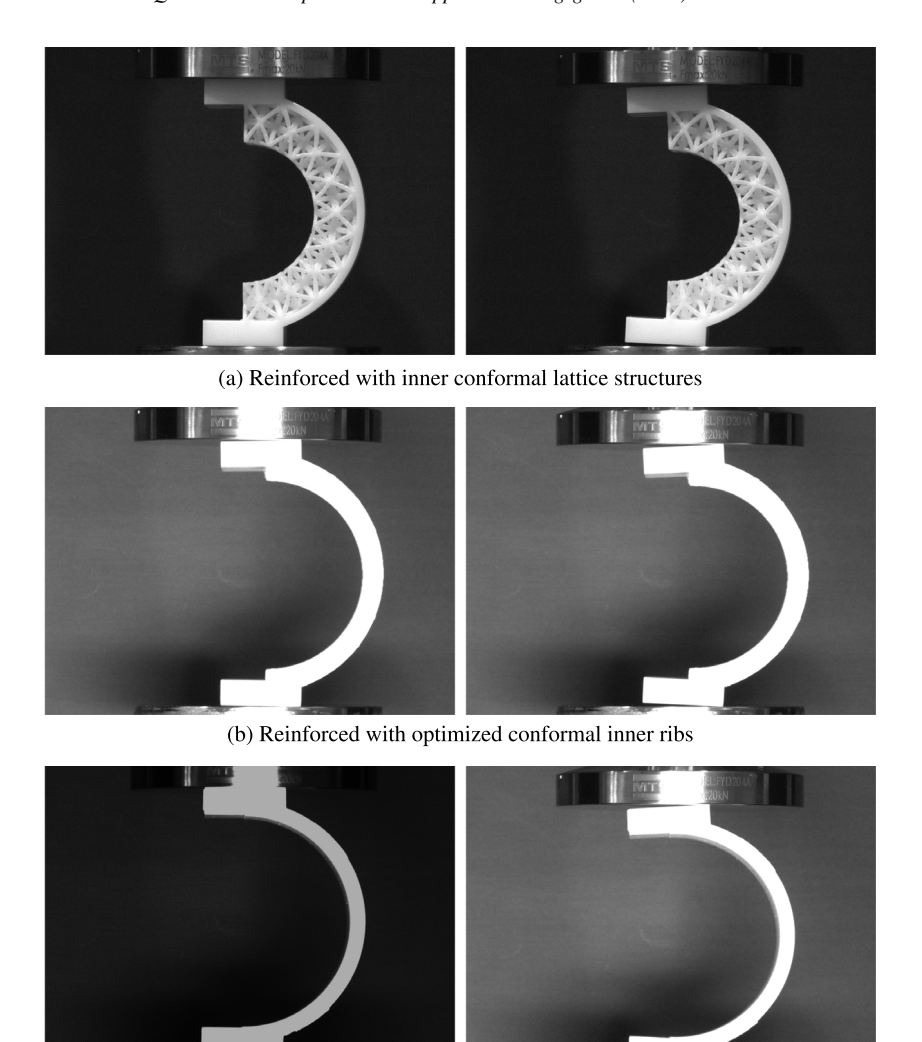
Fig. 15. Semi-cylindrical designs with different reinforcing structures: (A). reinforced with inner conformal lattice structure, (B). reinforced with optimized inner ribs, (C). uniform thickness design.

optimized inner ribs, and uniform thickness, respectively. The compression test is operated by the MTS Model 43 testing system. The specimens are loosely placed vertically between the two compression platens, and then the upper compression platen moves downward with a constant speed of 0.085 mm/s, at the meantime, the reaction force made by the specimens is recorded every 0.001 s. Fig. 16 shows the initial placement of the semi-cylinder shells and their corresponding status with 3 mm vertical deformation. The reaction force vs. deformation plots for semi-cylinder designs with different reinforcing structures is shown in Fig. 17. The *x*-axis represents the deformation rate, and the *y*-axis denotes the reaction force. This chart demonstrates that at every deformation rate, the semi-cylinder reinforced with ribs generates higher reaction force than the other two designs, while the semi-cylinder with uniform thickness shows the lowest reaction force. As seen, the slope of the plot of the surface with inner optimized ribs is the steepest among the three. Specifically, by increasing the deformation, the reaction force of the rib-reinforced semi-cylinder surface rises more quickly, which indicates the rib-reinforced structure possesses higher stiffness under the same deformation compared with the other two designs. In general, we can conclude that both the rib-reinforces structures and the conformal lattice structures can increase the stiffness of the semi-cylinder shell.

8. Conclusions

In this paper, we propose a new computational framework for structural shape and topology optimization on manifolds. By employing the conformal mapping theory, we extend the level-set-based topology optimization approach from the Euclidean space \mathbb{R}^2 or \mathbb{R}^3 to surfaces with arbitrary topologies. Following the conformal geometry theory, we can conformally map a manifold onto a 2D rectangle plane, where the level set function is defined. With conformal mapping, the corresponding covariant derivatives on a manifold can be represented by the Euclidean differential operators multiplied by a scalar. Therefore, the topology optimization problem on a free-form surface can be formulated as a 2D problem in the Euclidean space. To evolve the boundaries on a free-form surface, we propose a modified Hamilton–Jacobi equation and solve it on the 2D plane. In this way, we can fully utilize the conventional computational schemes for level set methods. Compared with other established approaches, the computational complexity of our method is highly reduced, while all the advantages of conventional level set methods are well preserved. The numerical experiments results indicate the robustness and effectiveness of X-LSM in solving topology optimization problems on manifolds.

Although the minimum compliance problem is studied in this paper to verify the performance of the proposed method in handling shape and topology optimization on free-form surfaces. The framework can be easily extended to other applications. For instance, to improve the antenna performances [69], one can use the X-LSM to optimize the conductive material distribution on the surface of the substrate. Moreover, because of the unique advantage of the conformal mapping theory that reveals the intrinsic geometric relationship between the surface and its conformal 2D domain, we can apply the X-LSM to optimize the deformation demanded surfaces, for example, the stretchable circuits [70,71], conformal electronics [3] and the metamaterial absorber on curved surfaces [72]. In addition, the X-LSM are also desirable for designing soft robotics on shell or plate. For instance, Shian and Betoldi et al. [73] illustrated the dielectric elastomer based gripper designs by placing a few stiff fibers into voltage-actuated dielectric elastomer beams. With the X-LSM, one can optimize the fibers' location and design the gripper without intuitions or inspirations. Further work will be focused on the generative structural designs on free-form surfaces for the above-mentioned problems.



(c) Reference design with uniform thickness

Fig. 16. Semi-cylindrical designs with different reinforcing structures: before deformation (left), and 3 mm vertical displacement load (right).

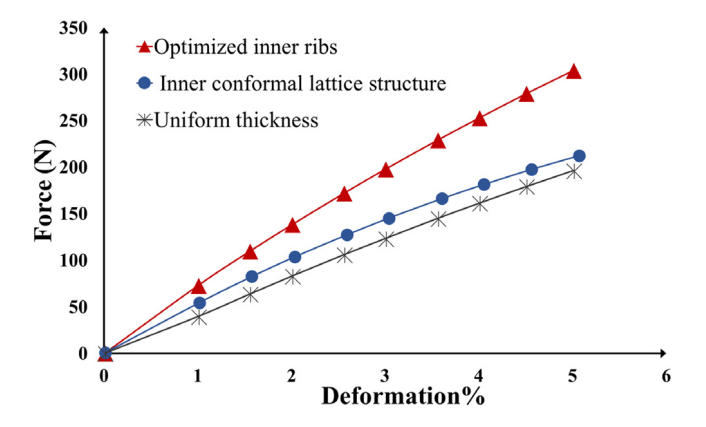


Fig. 17. Force-deformation curve for semi-cylinders with different reinforcing structures.

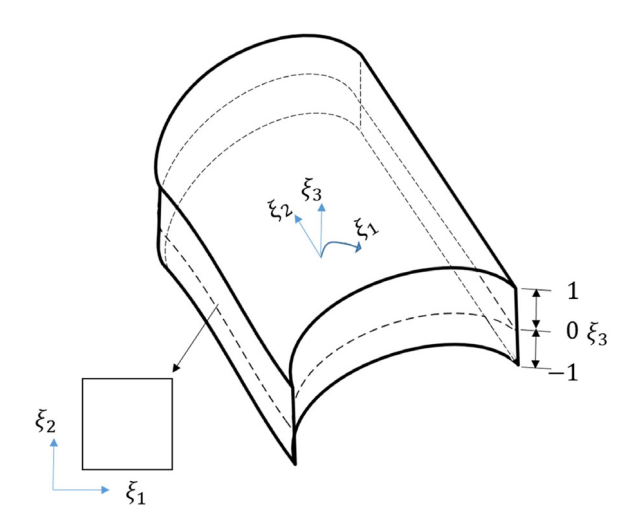


Fig. 18. The schematic figure of shell structure.

Acknowledgments

This work is supported by the National Science Foundation (CMMI-1462270 and CMMI-1762287), the Ford University Research Program (URP), and the start-up fund from the State University of New York at Stony Brook. We are grateful to Prof. Ole Sigmund and Prof. Kurt Maute for their insightful comments on the experiment on the semi-cylindrical designs at the 2018 Sandia Topology Optimization Roundtable. We would also like to thank Dr. Tiantian Li for his assistance with the experimental work.

Appendix A. The strain energy density of a linear elastic shell structure

In this section, the background information of the linear elastic shell structure is introduced, and the derivation of the strain energy density is derived. Typically, a shell structure consists of a curved external surface as well as a uniform thickness, as shown in Fig. 18. Let ξ_1 , ξ_2 be the two curvilinear coordinates in the middle surface, and ξ_3 be the coordinate in the thickness direction varying within $[-1\ 1]\ [74,75]$. Thus, any point on the shell structure can be represented as $x(\xi_1, \xi_2, \xi_3)\ [76,77]$.

$$\mathbf{x}(\xi_1, \xi_2, \xi_3) = \mathbf{x}^n(\xi_1, \xi_2) + \xi_3 \frac{t(\xi_1, \xi_2)}{2} \mathbf{n}(\xi_1, \xi_2). \tag{23}$$

The Jacobian matrix of the mapping between the physical coordinates and the reference coordinates is

$$J = \frac{\partial x_i}{\partial \xi_i}.$$
 (24)

For linear elastic material, the strain tensor is defined as

$$\epsilon_{ij}(u) = \frac{1}{2} \left(\frac{\partial u_i}{\partial x_j} + \frac{\partial u_j}{\partial x_i} \right),$$

$$\epsilon_{ij}(u) = \frac{1}{2} \left(\frac{\partial u_i}{\partial \xi_m} \frac{\partial \xi_m}{\partial x_j} + \frac{\partial u_j}{\partial \xi_m} \frac{\partial \xi_m}{\partial x_i} \right),$$
(25)

$$\epsilon_{ij}(u) = \frac{1}{2} \left(\frac{\partial u_i}{\partial \xi_m} \frac{1}{J_{mj}} + \frac{\partial u_j}{\partial \xi_m} \frac{1}{J_{mi}} \right)$$

$$= sym(\frac{\partial u_i}{\partial \xi_m} J_{mj}^{-1}),$$
(26)

where ξ_m represents the reference coordinates. The energy bilinear form for linear elasticity is shown as

$$a(u,v) = \int_{\Omega} \epsilon_{ij}(u) \mathbb{C}_{ijkl} \epsilon_{kl}(v) d\Omega, \tag{27}$$

where u stands for the displacement, and v is the test function.

According to the Reissner–Mindlin theory of plate [78], we can assume that the displacement along the thickness is linear and the cross section of the shell structure remains flat after deformation. Then the deformation on shell can be written as [79]

$$u = u^{1}(\xi_{1}, \xi_{2}) + \xi_{3}u^{2}(\xi_{1}, \xi_{2}), \tag{28}$$

where on the right-hand side, the first term represents the membrane deformation, and the second term stands for the bending and shear deformation.

For the thin shell which the thickness is very small and can be neglected, the Jacobian is considered to be a function of only ξ_1 , ξ_2 coordinates. Thus Eq. (26) can be simplified as [79]:

$$\epsilon_{ij}(u) = \epsilon_{ij}^{1}(u) + \xi_{3}\epsilon_{ij}^{2}(u), \tag{29}$$

where $\epsilon_{ii}^1(u)$ and $\epsilon_{ii}^2(u)$ are the membrane-shear stain and bending strain respectively.

Substitute Eq. (29) into Eq. (27) and integrate from $\xi_3 \in [-1, 1]$, we can rewrite the energy bilinear form as [63,79]

$$a(u, v) = \int_{-1}^{1} \iint [\epsilon_{ij}^{1}(u) + \xi_{3}\epsilon_{ij}^{2}(u)] \mathbb{C}_{ijkl}[\epsilon_{ij}^{1}(v) + \xi_{3}\epsilon_{ij}^{2}(v)] |\mathbf{J}| d\xi_{1} d\xi_{2} d\xi_{3}$$

$$= \int_{-1}^{1} \iint [\epsilon_{ij}^{1}(u) \mathbb{C}_{ijkl}\epsilon_{ij}^{1}(v) + \xi_{3}\epsilon_{ij}^{1}(u) \mathbb{C}_{ijkl}\epsilon_{ij}^{2}(v)$$

$$+ \xi_{3}\epsilon_{ij}^{2}(u) \mathbb{C}_{ijkl}\epsilon_{ij}^{1}(v) + \xi_{3}^{2}\epsilon_{ij}^{2}(u) \mathbb{C}_{ijkl}\epsilon_{ij}^{2}(v)] |\mathbf{J}| d\xi_{1} d\xi_{2} d\xi_{3}.$$
(30)

since the second and third terms are odd functions over the interval $\xi_3 \in [-1, 1]$, and thus Eq. (30) can be simplified as below [63]

$$a(u,v) = \int_{A} [2\epsilon_{ij}^{1}(u)\mathbb{C}_{ijkl}\epsilon_{kl}^{1}(v)|\mathbf{J}| + \frac{2}{3}\epsilon_{ij}^{2}(u)\mathbb{C}_{ijkl}\epsilon_{kl}^{2}(v)|\mathbf{J}|]dA.$$
(31)

Appendix B. Discrete surface Ricci flow

Practically, surfaces are represented as triangular meshes. A discrete metric on a mesh is the edge length function, denoted as $l: E \to \mathbb{R}^+$, which satisfies the triangle inequality. The discrete Gauss curvature is the angle deficit, defined on vertices, $K: V \to \mathbb{R}$,

$$K(v) = \begin{cases} 2\pi - \sum_{jk} \theta_i^{jk}, & v \notin \partial M \\ \pi - \sum_{jk} \theta_i^{jk}, & v \in \partial M \end{cases}, \tag{32}$$

where θ_i^{jk} is the corner angle at v_i in the face $[v_i, v_j, v_k]$, and ∂M represents the boundary of the mesh.

The discrete Gaussian curvature is determined by the discrete Riemannian metric via the cosine law,

$$l_i^2 = l_i^2 + l_k^2 - 2l_i l_k \cos \theta_i. \tag{33}$$

The Gauss–Bonnet theorem still holds in the discrete case. The total curvature equals the product of 2π and the Euler characteristic number χ ,

$$\sum_{v \notin \partial M} K(v) + \sum_{v \in \partial M} K(v) = 2\pi \chi(M). \tag{34}$$

The cotangent edge weight plays an important role. Given an interior edge $[v_i, v_j]$ adjacent to two faces $[v_i, v_j, v_k]$ and $[v_j, v_i, v_l]$, the cotangent weight is defined as

$$w_{ij} = \cot \theta_k^{ij} + \cot \theta_l^{ji}. \tag{35}$$

If the edge is on the boundary, adjacent to the face $[v_i, v_i, v_k]$, then the cotangent weight is

$$w_{ij} = \cot \theta_k^{ij}. \tag{36}$$

A triangulation of the mesh is called *Delaunay*, if all cotangent edge weights are non-negative.

Given a triangular mesh M, the discrete conformal factor is a function defined on each vertex $\mathbf{u}: V \to \mathbb{R}$, and the length of an edge $[v_i, v_j]$ is given by

$$l_{ij} = \exp(u_i)\beta_{ij}\exp(u_j),\tag{37}$$

where β_{ij} is the initial edge length.

Definition B.1 (Discrete Surface Ricci Flow). The discrete surface Ricci flow is defined as

$$\frac{du_i(t)}{dt} = \bar{K}_i - K_i(t),\tag{38}$$

where K_i is the target curvature at the vertex v_i , and the discrete metric is given in Eq. (37). During the flow, the triangulation is updated to be Delaunay.

The existence of the Ricci flow has recently been proved in [80].

Theorem B.2 (Discrete Uniformization [81,82]). Given a target curvature \bar{K} satisfying the Gauss–Bonnet condition in Eq. (34), and for each vertex $\bar{K}_i \in (-\infty, 2\pi)$, then there exists a solution to the Ricci flow equation (38). The solution is unique up to a constant.

Furthermore, the discrete Ricci flow is the negative gradient flow of the discrete Ricci energy:

$$E_{\Sigma}(\mathbf{u}) = \int_{i-1}^{\mathbf{u}} \sum_{i-1}^{n} (\bar{K}_i - K_i) du_i.$$
(39)

References

- [1] S. Adriaenssens, P. Block, D. Veenendaal, C. Williams, Shell structures for architecture: form finding and optimization, Routledge, 2014.
- [2] H.C. Ko, G. Shin, S. Wang, M.P. Stoykovich, J.W. Lee, D.-H. Kim, J.S. Ha, Y. Huang, K.-C. Hwang, J.A. Rogers, Curvilinear electronics formed using silicon membrane circuits and elastomeric transfer elements, Small 5 (23) (2009) 2703–2709.
- [3] H.C. Ko, M.P. Stoykovich, J. Song, V. Malyarchuk, W.M. Choi, C.-J. Yu, J.B. Geddes Iii, J. Xiao, S. Wang, Y. Huang, et al., A hemispherical electronic eye camera based on compressible silicon optoelectronics, Nature 454 (7205) (2008) 748.
- [4] J.-H. Zhu, W.-H. Zhang, L. Xia, Topology optimization in aircraft and aerospace structures design, Arch. Comput. Methods Eng. 23 (4) (2016) 595–622.
- [5] E. Lund, J. Stegmann, On structural optimization of composite shell structures using a discrete constitutive parametrization, Wind Energy 8 (1) (2005) 109–124.
- [6] E. Lund, Buckling topology optimization of laminated multi-material composite shell structures, Compos. Struct. 91 (2) (2009) 158–167.
- [7] J. Stegmann, E. Lund, Discrete material optimization of general composite shell structures, Internat. J. Numer. Methods Engrg. 62 (14) (2005) 2009–2027.
- [8] K. Suzuki, N. Kikuchi, A homogenization method for shape and topology optimization, Comput. Methods Appl. Mech. Engrg. 93 (3) (1991) 291–318.
- [9] G. Allaire, R. Kohn, Topology optimization and optimal shape design using homogenization, in: Topology Design of Structures, Springer, 1993, pp. 207–218.
- [10] S. Nishiwaki, M.I. Frecker, S. Min, N. Kikuchi, Topology optimization of compliant mechanisms using the homogenization method, Internat. J. Numer. Methods Engrg. 42 (3) (1998) 535–559.
- [11] G.I. Rozvany, M. Zhou, T. Birker, Generalized shape optimization without homogenization, Struct. Optim. 4 (3-4) (1992) 250-252.
- [12] M.P. Bendsoe, O. Sigmund, Topology optimization: theory, methods, and applications, Springer Science & Business Media, 2013.
- [13] E. Fauche, S. Adriaenssens, J.H. Prevost, Structural optimization of a thin-shell bridge structure, J. Int. Assoc. Shell Spat. Struct. 51 (2) (2010) 153.
- [14] M. Papadrakakis, V. Papadopoulos, G. Stefanou, V. Plevris, Shape-topology optimization for designing shell structures.
- [15] R. Ansola, J. Canales, J.A. Tarrago, J. Rasmussen, An integrated approach for shape and topology optimization of shell structures, Comput. Struct. 80 (5–6) (2002) 449–458.
- [16] R. Ansola, J. Canales, J. Tarrago, J. Rasmussen, Combined shape and reinforcement layout optimization of shell structures, Struct. Multidiscip. Optim. 27 (4) (2004) 219–227.

- [17] B. Hassani, S.M. Tavakkoli, H. Ghasemnejad, Simultaneous shape and topology optimization of shell structures, Struct. Multidiscip. Optim. 48 (1) (2013) 221–233.
- [18] O. Sigmund, J. Petersson, Numerical instabilities in topology optimization: a survey on procedures dealing with checkerboards, mesh-dependencies and local minima, Struct. Optim. 16 (1) (1998) 68–75.
- [19] C.-Y. Lin, L.-S. Chao, Automated image interpretation for integrated topology and shape optimization, Struct. Multidiscip. Optim. 20 (2) (2000) 125–137.
- [20] Y.-L. Hsu, M.-S. Hsu, C.-T. Chen, Interpreting results from topology optimization using density contours, Comput. Struct. 79 (10) (2001) 1049–1058.
- [21] A. Yildiz, N. Öztürk, N. Kaya, F. Öztürk, Integrated optimal topology design and shape optimization using neural networks, Struct. Multidiscip. Optim. 25 (4) (2003) 251–260.
- [22] S. Chu, M. Xiao, L. Gao, L. Gui, H. Li, An effective structural boundary processing method based on support vector machine for discrete topology optimization, in: Computer Supported Cooperative Work in Design (CSCWD), 2016 IEEE 20th International Conference on, IEEE, 2016, pp. 10–15.
- [23] J.K. Guest, J.H. Prévost, T. Belytschko, Achieving minimum length scale in topology optimization using nodal design variables and projection functions, Internat. J. Numer. Methods Engrg. 61 (2) (2004) 238–254.
- [24] T.A. Poulsen, A new scheme for imposing a minimum length scale in topology optimization, Internat. J. Numer. Methods Engrg. 57 (6) (2003) 741–760.
- [25] X. Guo, W. Zhang, W. Zhong, Doing topology optimization explicitly and geometrically anew moving morphable components based framework, J. Appl. Mech. 81 (8) (2014) 081009.
- [26] X. Guo, W. Zhang, J. Zhang, J. Yuan, Explicit structural topology optimization based on moving morphable components (MMC) with curved skeletons, Comput. Methods Appl. Mech. Engrg. 310 (2016) 711–748.
- [27] W. Zhang, J. Yuan, J. Zhang, X. Guo, A new topology optimization approach based on Moving Morphable Components (MMC) and the ersatz material model, Struct. Multidiscip. Optim. 53 (6) (2016) 1243–1260.
- [28] W. Zhang, W. Yang, J. Zhou, D. Li, X. Guo, Structural topology optimization through explicit boundary evolution, J. Appl. Mech. 84 (1) (2017) 011011.
- [29] J. Norato, B. Bell, D. Tortorelli, A geometry projection method for continuum-based topology optimization with discrete elements, Comput. Methods Appl. Mech. Engrg. 293 (2015) 306–327.
- [30] S. Zhang, J.A. Norato, A.L. Gain, N. Lyu, A geometry projection method for the topology optimization of plate structures, Struct. Multidiscip. Optim. 54 (5) (2016) 1173–1190.
- [31] S. Zhang, A.L. Gain, J.A. Norato, Stress-based topology optimization with discrete geometric components, Comput. Methods Appl. Mech. Engrg. 325 (2017) 1–21.
- [32] G. Allaire, F. Jouve, A.-M. Toader, Structural optimization using sensitivity analysis and a level-set method, J. Comput. Phys. 194 (1) (2004) 363–393.
- [33] S.J. Osher, F. Santosa, Level set methods for optimization problems involving geometry and constraints: I. frequencies of a two-density inhomogeneous drum, J. Comput. Phys. 171 (1) (2001) 272–288.
- [34] G. Allaire, F. Jouve, A.-M. Toader, A level-set method for shape optimization, C. R. Math. 334 (12) (2002) 1125-1130.
- [35] M.Y. Wang, X. Wang, D. Guo, A level set method for structural topology optimization, Comput. Methods Appl. Mech. Engrg. 192 (1–2) (2003) 227–246.
- [36] P. Vogiatzis, S. Chen, C. Zhou, An open source framework for integrated additive manufacturing and level-set-based topology optimization, J. Comput. Inf. Sci. Eng. 17 (4) (2017) 041012.
- [37] M.Y. Wang, X. Wang, PDE-driven level sets, shape sensitivity and curvature flow for structural topology optimization, Comput. Model. Eng. Sci. 6 (2004) 373–396.
- [38] L. Lopez-Perez, R. Deriche, N. Sochen, The Beltrami flow over triangulated manifolds, in: Computer Vision and Mathematical Methods in Medical and Biomedical Image Analysis, Springer, 2004, pp. 135–144.
- [39] U. Clarenz, M. Rumpf, A. Telea, Surface processing methods for point sets using finite elements, Comput. Graph. 28 (6) (2004) 851–868.
- [40] L. Dedè, A. Quarteroni, Isogeometric analysis for second order partial differential equations on surfaces, Comput. Methods Appl. Mech. Engrg. 284 (2015) 807–834.
- [41] A. Bartezzaghi, L. Dedè, A. Quarteroni, Isogeometric analysis of high order partial differential equations on surfaces, Comput. Methods Appl. Mech. Engrg. 295 (2015) 446–469.
- [42] S.J. Ruuth, B. Merriman, A simple embedding method for solving partial differential equations on surfaces, J. Comput. Phys. 227 (3) (2008) 1943–1961.
- [43] M. Bertalmio, L.-T. Cheng, S. Osher, G. Sapiro, Variational problems and partial differential equations on implicit surfaces, J. Comput. Phys. 174 (2) (2001) 759–780.
- [44] N.D. King, S.J. Ruuth, Solving variational problems and partial differential equations that map between manifolds via the closest point method, J. Comput. Phys. 336 (2017) 330–346.
- [45] C.B. Macdonald, S.J. Ruuth, Level set equations on surfaces via the Closest Point Method, J. Sci. Comput. 35 (2–3) (2008) 219–240.
- [46] M. Bertalmio, G. Sapiro, G. Randall, Region tracking on level-sets methods, IEEE Trans. Med. Imaging 18 (5) (1999) 448-451.
- [47] F. Mémoli, G. Sapiro, S. Osher, Solving variational problems and partial differential equations mapping into general target manifolds, J. Comput. Phys. 195 (1) (2004) 263–292.
- [48] S. Chen, W. Chen, A new level-set based approach to shape and topology optimization under geometric uncertainty, Struct. Multidiscip. Optim. 44 (1) (2011) 1–18.

- [49] J.-P. Pons, G. Hermosillo, R. Keriven, O. Faugeras, Maintaining the point correspondence in the level set framework, J. Comput. Phys. 220 (1) (2006) 339–354.
- [50] X. Gu, S. Wang, J. Kim, Y. Zeng, Y. Wang, H. Qin, D. Samaras, Ricci flow for 3D shape analysis, in: Computer Vision, 2007. ICCV 2007. IEEE 11th International Conference on, IEEE, 2007, pp. 1–8.
- [51] X. Gu, Y. Wang, T.F. Chan, P.M. Thompson, S.-T. Yau, Genus zero surface conformal mapping and its application to brain surface mapping, IEEE Trans. Med. Imaging 23 (8) (2004) 949–958.
- [52] L.M. Lui, X. Gu, T.F. Chan, S.-T. Yau, et al., Variational method on Riemann surfaces using conformal parameterization and its applications to image processing, Methods Appl. Anal. 15 (4) (2008) 513–538.
- [53] X. Gu, S.-T. Yau, Computational conformal geometry, Higher Education Press, 2008.
- [54] L.M. Lui, Y. Wang, T.F. Chan, Solving PDEs on manifolds with global conformal parametriazation, in: Variational, Geometric, and Level Set Methods in Computer Vision, Springer, 2005, pp. 307–319.
- [55] S. Osher, J.A. Sethian, Fronts propagating with curvature-dependent speed: algorithms based on Hamilton-Jacobi formulations, J. Comput. Phys. 79 (1) (1988) 12–49.
- [56] S. Osher, R. Fedkiw, Level set methods and dynamic implicit surfaces, Springer, 2003.
- [57] J.A. Sethian, Level set methods and fast marching methods: evolving interfaces in computational geometry, Fluid Mechanics, Computer Vision, and Materials Science, Vol. 3, Cambridge university press, 1999.
- [58] X.D. Gu, S.-T. Yau, Computational conformal geometry, International Press Somerville, Mass, USA, 2008.
- [59] R. Hamilton, The Ricci flow on surfaces, Mathematics and general relativity (Santa Cruz, CA, 1986), 237–262, Contemp. Math. 71 (1988) 301–307.
- [60] W. Zeng, X. Gu, Ricci flow for shape analysis and surface registration: theories, algorithms, and applications, Springer Science & Business Media, 2013.
- [61] D.X. Gu, W. Zeng, F. Luo, S.-T. Yau, Numerical computation of surface conformal mappings, Comput. Methods Funct. Theory 11 (2) (2011) 747–787
- [62] J.M. Lee, Riemannian manifolds: an introduction to curvature, Vol. 176, Springer Science & Business Media, 2006.
- [63] K.K. Choi, N.-H. Kim, Structural sensitivity analysis and optimization 1: linear systems,, Springer Science & Business Media, 2006.
- [64] F. Chen, Y. Wang, M.Y. Wang, Y. Zhang, Topology optimization of hyperelastic structures using a level set method, J. Comput. Phys. 351 (2017) 437–454.
- [65] X. Guo, W. Zhang, W. Zhong, Stress-related topology optimization of continuum structures involving multi-phase materials, Comput. Methods Appl. Mech. Engrg. 268 (2014) 632–655.
- [66] Q. Xia, T. Shi, Optimization of structures with thin-layer functional device on its surface through a level set based multiple-type boundary method, Comput. Methods Appl. Mech. Engrg. 311 (2016) 56–70.
- [67] T. Belytschko, W.K. Liu, B. Moran, K. Elkhodary, Nonlinear finite elements for continua and structures, John wiley & sons, 2013.
- [68] P. Vogiatzis, M. Ma, S. Chen, X.D. Gu, Computational design and additive manufacturing of periodic conformal metasurfaces by synthesizing topology optimization with conformal mapping, Comput. Methods Appl. Mech. Engrg. 328 (2018) 477–497.
- [69] A. Erentok, O. Sigmund, Three-dimensional topology optimized electrically-small conformal antenna, in: Antennas and Propagation Society International Symposium, 2008. AP-S 2008. IEEE, IEEE, 2008, pp. 1–4.
- [70] D.-H. Kim, J.-H. Ahn, W.M. Choi, H.-S. Kim, T.-H. Kim, J. Song, Y.Y. Huang, Z. Liu, C. Lu, J.A. Rogers, Stretchable and foldable silicon integrated circuits, Science 320 (5875) (2008) 507–511.
- [71] S. Xu, Y. Zhang, J. Cho, J. Lee, X. Huang, L. Jia, J.A. Fan, Y. Su, J. Su, H. Zhang, et al., Stretchable batteries with self-similar serpentine interconnects and integrated wireless recharging systems, Nat. Commun. 4 (2013) 1543.
- [72] Y. Jang, M. Yoo, S. Lim, Conformal metamaterial absorber for curved surface, Opt. Express 21 (20) (2013) 24163–24170.
- [73] S. Shian, K. Bertoldi, D.R. Clarke, Dielectric elastomer based "grippers" for soft robotics, Adv. Mater. 27 (43) (2015) 6814–6819.
- [74] J. Zhu, The Finite Element Method: Its Basis and Fundamentals, Elsevier, 2013.
- [75] O.C. Zienkiewicz, R.L. Taylor, The finite element method for solid and structural mechanics, Elsevier, 2005.
- [76] P.G. Ciarlet, An introduction to differential geometry with applications to elasticity, J. Elasticity 78 (1–3) (2005) 1–215.
- [77] D. Chapelle, K.-J. Bathe, The finite element analysis of shells-fundamentals, Springer Science & Business Media, 2010.
- [78] P. Papadopoulos, R.L. Taylor, A triangular element based on Reissner-Mindlin plate theory, Internat. J. Numer. Methods Engrg. 30 (5) (1990) 1029–1049.
- [79] N.H. Kim, K.K. Choi, J.-S. Chen, M.E. Botkin, Meshfree analysis and design sensitivity analysis for shell structures, Internat. J. Numer. Methods Engrg. 53 (9) (2002) 2087–2116.
- [80] B. Chow, F. Luo, et al., Combinatorial Ricci flows on surfaces, J. Differential Geom. 63 (1) (2003) 97–129.
- [81] X.D. Gu, F. Luo, J. Sun, T. Wu, et al., A discrete uniformization theorem for polyhedral surfaces, J. Differential Geom. 109 (2) (2018) 223–256.
- [82] X. Gu, R. Guo, F. Luo, J. Sun, T. Wu, et al., A discrete uniformization theorem for polyhedral surfaces II, J. Differential Geom. 109 (3) (2018) 431–466.